

# One-Pot Hydrothermal Synthesis of Reduced Graphene Oxide–Multiwalled Carbon Nanotubes Composite Material on Nickel Foam for Efficient Supercapacitor Electrode

Fook Yun Ban<sup>1</sup> · Subramaniam Jayabal<sup>1</sup> · Alagarsamy Pandikumar<sup>1</sup> · Hong Ngee Lim<sup>2</sup> · Nay Ming Huang<sup>1</sup>

Published online: 11 April 2015  
© Springer Science+Business Media New York 2015

**Abstract** The reduced graphene oxide/multiwalled carbon nanotubes deposited on nickel foam (rGO/MWCNTs/NF) composite material was successfully prepared using one-pot hydrothermal method. The prepared rGO/MWCNTs/NF composite material was characterized using scanning electron microscopy, electron dispersive spectroscopy, and Raman spectroscopy. The results show that MWCNTs were successfully incorporated into the graphene sheets uniformly. The rGO/MWCNTs/NF composite material was fabricated as electrode for supercapacitor application. The capacitive properties of the rGO/MWCNTs/NF composite material were studied using electrochemical impedance spectroscopy, cyclic voltammetry, and galvanostatic charge/discharge in 1 M KOH aqueous electrolyte solution. The rGO/MWCNTs/NF electrode showed enhanced capacitance compared to rGO/NF, MWCNTs/NF, and bare NF electrodes due to high surface area and more accessibility of electrolyte after the addition of MWCNTs to the rGO/NF electrode. The rGO/MWCNTs/NF composite material shows specific capacitance of 81.14 F g<sup>-1</sup> at current density of 1 A g<sup>-1</sup> and excellent cycling stability with 83 % of its initial capacitance after 1000 charge/discharge cycles.

**Keywords** Reduced graphene oxide · Multiwalled carbon nanotubes · Nickel foam · Supercapacitor

✉ Nay Ming Huang  
huangnayingming@gmail.com

<sup>1</sup> Low Dimensional Materials Research Centre, Department of Physics, Faculty of Science, University of Malaya, 50603 Kuala Lumpur, Malaysia

<sup>2</sup> Department of Chemistry, Faculty of Science and Functional Device Laboratory, Institute of Advanced Technology, Universiti Putra Malaysia, 43400 UPM Serdang, Selangor, Malaysia

## Introduction

Electrochemical supercapacitors are electrical energy storage devices emerging as one of the potential energy storage devices used in the portable electronics, smart grids, and hybrid electric vehicles in recent years due to their high power density, reversibility, long life cycle, a wide thermal operating range, flexible packaging, low maintenance, and small environmental impact [1, 2]. There are two basic types of supercapacitor according to their charge storage mechanism, namely, (i) electric double-layer capacitor (EDLC) and (ii) *pseudo*-capacitor. EDLC generates capacitance from charge separation at the electrode/electrolyte interface, and therefore, it strongly depends on the surface area of the electrode material that is accessible to the electrolyte ions. *Pseudo*-capacitor generates capacitance from fast and reversible Faradic reactions involving the electrolyte and electroactive species on the electrode surface [1–7]. Although, the *pseudo*-capacitor-based devices have higher energy densities compared to EDLC-based devices, they suffer from the drawbacks of a low power density and lack of stability during potential cycling [2, 6].

Nickel foam (NF) was used as the current collector and supporting structure for the electrode material due to its high electronic conductivity, 3D open-pore structure, electrochemical inertness, relatively low toxicity, and low cost [8–11]. Thus, NF is used as a promising candidate for designing the electrode materials for electrochemical supercapacitor applications. Graphene, a one-atom-thick sheet of sp<sup>2</sup> bonded carbon atoms with a 2D honeycomb lattice structure, is emerging as a promising material for fabricating high-performance supercapacitors due to its low mass density, excellent electronic conductivity, high intrinsic strength, reasonable chemical stability, higher thermal conductivity, and high surface area [12–14]. Most of the synthesized graphene materials contain oxygen as the principle element, and they are called reduced

graphene oxide (rGO) [15, 16]. In recent years, graphene-based materials showed an enhanced electrochemical performance toward supercapacitor applications [12, 17–26]. However, the major problem with the use of graphene in supercapacitor is its tendency to restack through the vander Waals' interactions during the drying process, which effectively decreases the effective surface area and therefore reduces the performance of the supercapacitor [27, 28]. This problem is rectified by introducing spacers between the graphene sheets [27–30]. Carbon nanotubes act as spacer between graphene sheets which give rise to rapid diffusion pathways for the electrolyte ions and also act as binder to prevent restacking of graphene sheets. Moreover, it possesses high electronic conductivity and high surface area, which also increases the performance of the supercapacitor [27–31]. Therefore, the carbon-nanotube-incorporated graphene-based materials show an improved electrochemical performance for the supercapacitor applications when compared to the graphene materials [32–40]. The capacitance of a supercapacitor is strongly dependent on the cell configuration set used for the electrochemical measurement [41]. The two-electrode system gives most accurate measurement of the material performance for the supercapacitor when compared to a three-electrode system [41–43].

In the present work, we have employed a facile one-step hydrothermal method to deposit the reduced graphene oxide/multiwalled carbon nanotubes (rGO/MWCNTs) composite on the NF without using any binders. The rGO/MWCNTs deposited on the NF (rGO/MWCNTs/NF) was fabricated as electrode for supercapacitor application. The electrochemical characterization including cyclic voltammetry, cyclic charge-discharge, and electrochemical impedance spectroscopy techniques are studied. The fabricated rGO/MWCNTs/NF electrode exhibits improved specific capacitance behaviour with high rate capability and good electrochemical cyclic stability. The supercapacitor performance of rGO/MWCNTs/NF electrode was compared with rGO/NF, MWCNTs/NF, and bare NF electrodes.

## Experimental Section

### Materials

Graphite flakes were purchased from Ashbury Inc., USA. Sulfuric acid ( $\text{H}_2\text{SO}_4$ , 98 %), phosphoric acid ( $\text{H}_3\text{PO}_4$ , 85 %), potassium permanganate ( $\text{KMnO}_4$ , 99.9 %), and hydrogen peroxide ( $\text{H}_2\text{O}_2$ , 30 %) were purchased from Merck. Hydrogen chloride (HCl, 37 %) was purchased from Sigma-Aldrich. MWCNTs (>95 %) with outer diameter <8 nm and length of 10–30  $\mu\text{m}$  was purchased from Nova Scientific, Malaysia. The MWCNTs were used without any further treatment. Nickel form (NF) was purchased from American

Elements, USA (thickness 1.5 mm and size 500 mm  $\times$  500 mm). All other chemicals, unless otherwise specified, used in the present work were of analytical grade. All the glasswares were thoroughly cleaned with aqua regia (1:3 (v/v)  $\text{HNO}_3$ –HCl) (caution: aqua regia is a powerful oxidizing agent, and it should be handled with extreme care) and rinsed extensively with deionized water before use.

### Preparation of rGO/MWCNTs/NF Composite Material

Graphene oxide (GO) was synthesized from graphite powder using the modified Hummer method [44, 45]. A 3.0 mg/ml of GO solution was prepared and ultrasonicated for 30 min to obtain a homogeneous dispersity. The pH of the GO solution was adjusted to pH 7 using the 1 M KOH solution. Then, MWCNTs were added to that GO solution and allowed to stirring for 2 h in order to disperse the MWCNTs homogeneously. Then, the mixture was transferred to a 50-mL Teflon-lined autoclave together with the NF and subjected to hydrothermal treatment at 180  $^\circ\text{C}$  for 24 h. Finally, the prepared rGO/MWCNTs/NF composite materials were washed with ethanol followed by deionized water and dried at 60  $^\circ\text{C}$  for 2 h. For controlled experiment, the rGO-deposited NF (rGO/NF) electrode was prepared using the hydrothermal treatment method without MWCNTs and the MWCNT-deposited NF (MWCNTs/NF) electrode was also prepared using the hydrothermal treatment method without GO. Figure 1 shows the schematic diagram of one-step synthesis of the rGO/MWCNT composite material by hydrothermal process on the NF.

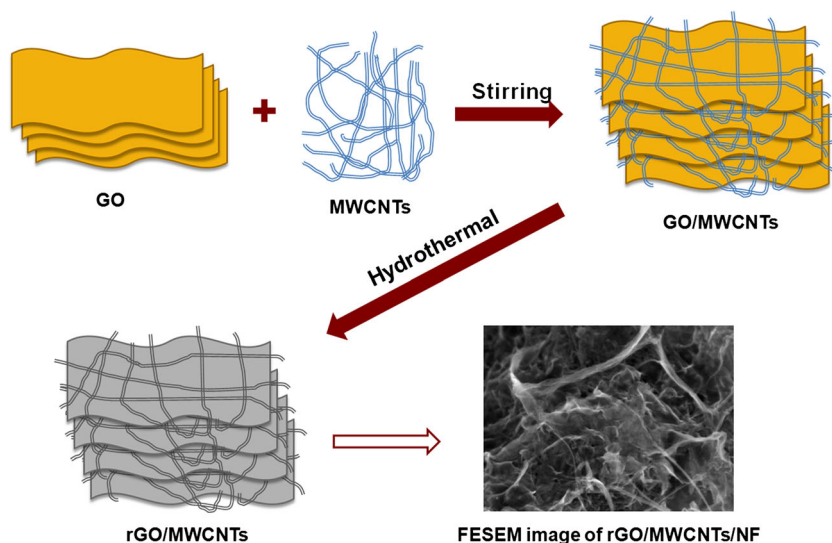
### Fabrication of Supercapacitor Test Cell

A two-electrode test cell was used for the measurement of performance of the supercapacitor because it gives most accurate measurement than the three-electrode cell. The obtained NF, rGO/NF, MWCNTs/NF, and rGO/MWCNTs/NF were used as electrodes for supercapacitor test cell. An aqueous solution of 1 M KOH was used as the electrolyte. The two identical NF or rGO/NF or MWCNTs/NF or rGO/MWCNTs/NF electrodes were assembled in a test cell, as shown in Fig. 2, which consists of two electrodes, and a separator. The filter paper is used as a separator during electrochemical measurements. Finally, the fabricated test cell was immersed in a beaker containing 1 M KOH electrolyte solution and used for the supercapacitor test cell.

### Characterization

The surface morphology of the rGO/MWCNTs/NF and bare NF electrodes were recorded using JEOL JEM-7600F field emission scanning electron microscopy. Raman spectra were recorded using a Renishaw 2000 inVia Raman microscope

**Fig. 1** Schematic diagram for the synthesis of rGO/MWCNTs materials by hydrothermal process



(Renishaw, UK) with a laser excitation source at 532 nm. All electrochemical experiments were carried out using a two-electrode system at 25 °C with 1 MKOH as the electrolyte solution. The electrochemical measurements such as cyclic voltammetry (CV), electrochemical impedance spectroscopy (EIS), and galvanostatic charge/discharge measurements were performed using Gamry Reference 600 electrochemical workstation (Gamry Instruments Inc., USA). EIS measurements were performed at open circuit potential over a frequency range of 0.01 Hz to 100 kHz.

The specific capacitance of the supercapacitor can be calculated from the cyclic voltammogram by using the equation [30, 42, 43]  $C_s = 4Q/m\Delta V_s$ , where  $C_s$  ( $F\ g^{-1}$ ) is the specific capacitance,  $Q$  (C) is the average charge during anodic and cathodic scan,  $m$  (g) is the mass of the active material in both electrodes,  $\Delta V$  (V) is the applied voltage window, and  $s$

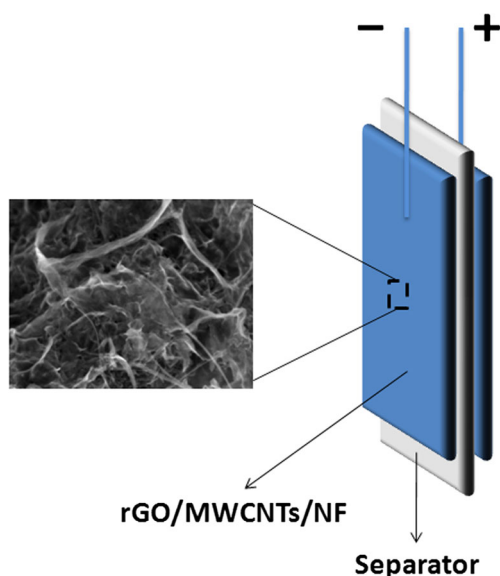


**Fig. 2** Schematic diagram of the supercapacitor test cell

( $V\ s^{-1}$ ) is the scan rate. The mass of the active material is calculated by taking into account the total mass of rGO/MWCNTs/NF, rGO/NF, and MWCNTs/NF by subtracting the weight of bare NF. The capacitance of bare NF electrode is very low when compared to capacitance of the rGO/MWCNTs/NF electrode (Fig. 7 (*vide infra*)). Such very small contribution of capacitance for bare NF electrode to the total capacitance is almost negligible [46, 47]. Therefore, for calculation of the mass of active material, we subtracted the mass of bare NF from the total mass of the rGO/MWCNTs/NF. The geometric surface area of the NF electrode is 2.5-cm length and 2.5-cm breadth. The specific capacitance of the supercapacitor can be calculated from the galvanostatic constant current discharge curves by using the equation [42]  $C_s = 4I/(dV/dt)m$ , where  $C_s$  ( $F\ g^{-1}$ ) is the specific capacitance,  $I$  (A) is discharge current,  $dV/dt$  is calculated from the slope of the constant current discharge curve, and  $m$  (g) is the total mass of the active material in both electrodes.

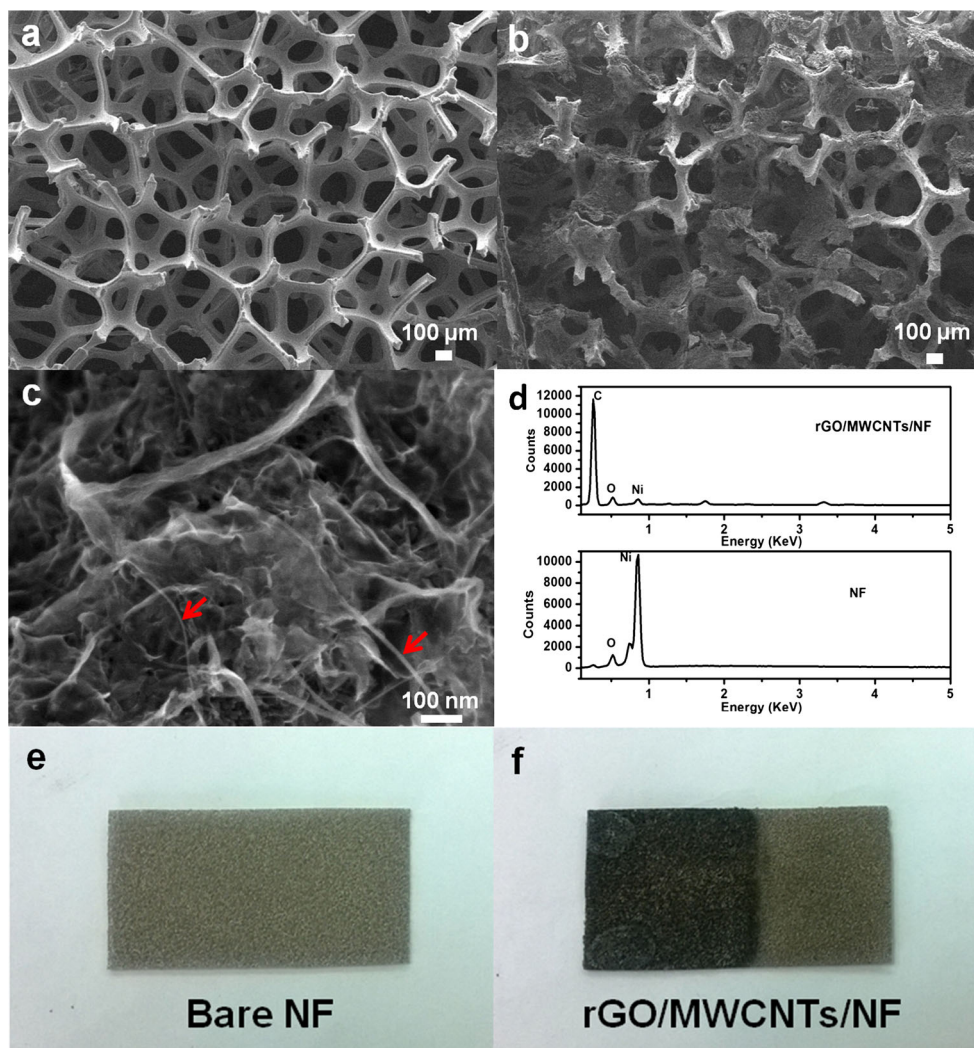
## Results and Discussion

### FESEM and TEM Analysis

The morphology of the bare NF and rGO/MWCNTs/NF composite material was examined by field emission scanning electron microscopy (FESEM). The FESEM image of bare NF (Fig. 3a) exhibits a porous structure with the pore size of 100–250  $\mu\text{m}$  and also have very smooth surface. This porous structure of NF allows other material to deposit over the surface. Figure 3b shows the FESEM image of rGO/MWCNTs/NF which indicates the successful deposition of rGO and MWCNTs on the porous NF structure. Figure 3c shows the FESEM image of rGO/MWCNTs/NF with higher magnification, which further confirms the uniform deposition of



**Fig. 3** FESEM images of bare NF (a), rGO/MWCNTs/NF electrodes at different magnifications (b, c), EDS analysis of bare NF and rGO/MWCNTs/NF (d), and photographs of bare NF and rGO/MWCNTs/NF



MWCNTs (marked in red arrow) and graphene sheets on the surface of porous NF structure. When GO is reduced by the hydrothermal treatment, the hydrophilic functional groups present in the GO are removed, which causes rGO sheets to restack [27, 28]. This can be avoided by using MWCNTs, which act as spacers to create gaps between adjacent graphene sheets and also enhance the accessibility electrolyte ions [27–30]. Here, the MWCNTs are adsorbed or sandwiched between the graphene layers through  $\pi$ - $\pi$  interactions between the graphene sheets and surface of MWCNTs, which helps to improve the electric conductivity of the composite material [27]. The unique structure with enhanced surface area of rGO/MWCNTs/NF composite material is useful for the improvement of capacitance performance. Figure 3d shows the EDS spectra of bare NF and rGO/MWCNTs/NF. The EDS spectrum rGO/MWCNTs/NF (Fig. 3d) shows the high intense peak for carbon compared to bare NF, indicating the formation of rGO/MWCNTs on the NF after hydrothermal treatment. Figure 3e, f shows the

photographs of bare NF and rGO/MWCNTs/NF. Figure 4 shows the TEM image of rGO/MWCNTs material which further confirms that MWCNTs (marked in red arrow) were inserted into graphene sheets.

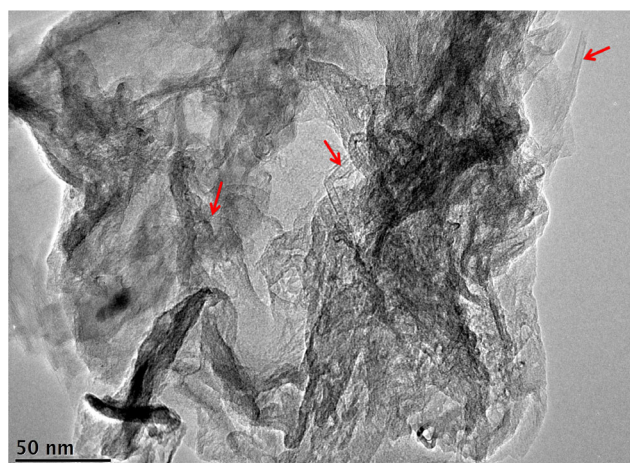


**Fig. 4** TEM image of rGO/MWCNTs

## Raman Analysis

The Raman spectra for rGO and rGO/MWCNTs composite material are shown in the Fig. 5. From Fig. 5, the Raman spectrum of rGO exhibit two prominent peaks at 1348 and 1593  $\text{cm}^{-1}$  corresponding to D and G bands [48] whereas Raman spectrum of rGO/MWCNTs composite material exhibits peaks at 1341 and 1574  $\text{cm}^{-1}$ . The relative intensity ratio of D band and G band ( $I_D/I_G$ ) for rGO/MWCNT composite material (0.41) is lower than the rGO (0.97), which indicates the disordered carbon structure in the rGO/MWCNT composite material. From Fig. 5, it is clearly seen that the Raman spectrum of rGO/MWCNT composite material exhibits sharp and intense peak at Raman shift of about 2672  $\text{cm}^{-1}$  corresponding to 2D band [48], whereas the Raman spectrum of rGO have small peak with low intensity at this region. The small peak of 2D band in the Raman spectrum of rGO indicates the graphene sheets restack back after hydrothermal treatment, and this 2D band in the Raman spectrum of rGO/MWCNTs becomes more prominence, which indicates the graphene sheets are well separated and prevented from restacking after the addition of MWCNTs.

## Electrochemical Testing

The EIS analysis has been one of the effective methods to study the electrochemical behavior of electrode materials for supercapacitors, and this technique provides an insight on the internal resistance of the electrode. Figure 6 shows the Nyquist plots of electrochemical impedance spectra recorded for rGO/MWCNTs/NF, rGO/NF, MWCNTs/NF, and bare NF electrodes in frequency range between 0.01 Hz and 1000 kHz at an open circuit potential of 10 mV. The rGO/MWCNTs/NF electrode have smaller semicircle in the high-frequency region (Fig. 6 (inset)) of the Nyquist plot as compared to the rGO/NF, MWCNTs/NF, and bare NF electrodes. This indicates that the

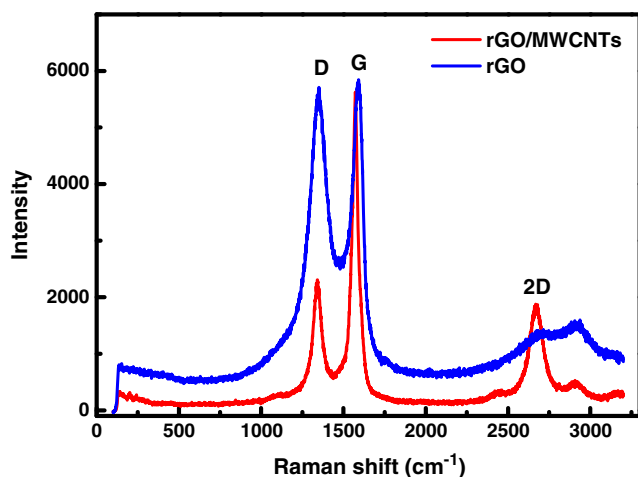


Fig. 5 Raman spectra of rGO and rGO/MWCNTs composite material

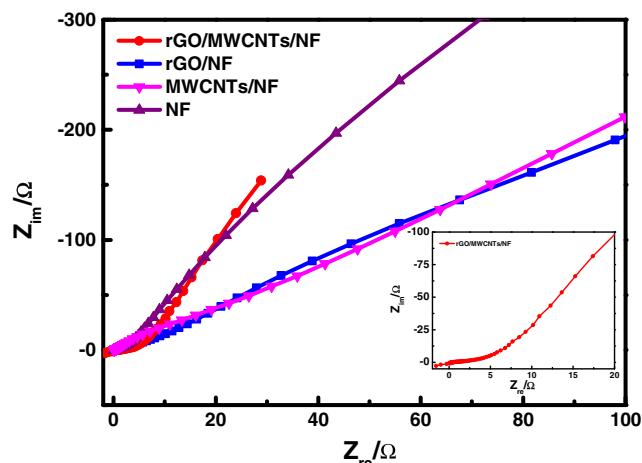


Fig. 6 Nyquist plot obtained for rGO/MWCNTs/NF, rGO/NF, MWCNTs/NF, and bare NF electrodes in frequency range between 0.01 Hz and 1000 kHz in 1 M KOH. Inset: enlarged Nyquist plot for rGO/MWCNTs/NF electrode

rGO/MWCNTs/NF electrode possess low electron transfer resistance, which suggests high charge transfer rate between the electrolyte and the active materials. The lower frequency part of the Nyquist plot represents the ability of ions to diffuse into the inner site of the electrode. The vertical shape of the rGO/MWCNTs/NF electrode indicates effective transport of ions behavior and thus shows enhanced electrochemical properties of the electrode.

The electrochemical performances of rGO/MWCNTs/NF, rGO/NF, MWCNTs/NF, and bare NF electrodes were examined by cyclic voltammetry. Figure 7 shows the cyclic voltammograms for rGO/MWCNTs/NF, rGO/NF, MWCNTs/NF, and bare NF electrodes in 1-M KOH solution at the scan rate of 100  $\text{mV s}^{-1}$ . From Fig. 7, the cyclic voltammogram of rGO/MWCNTs/NF electrode shows relatively rectangular in shape

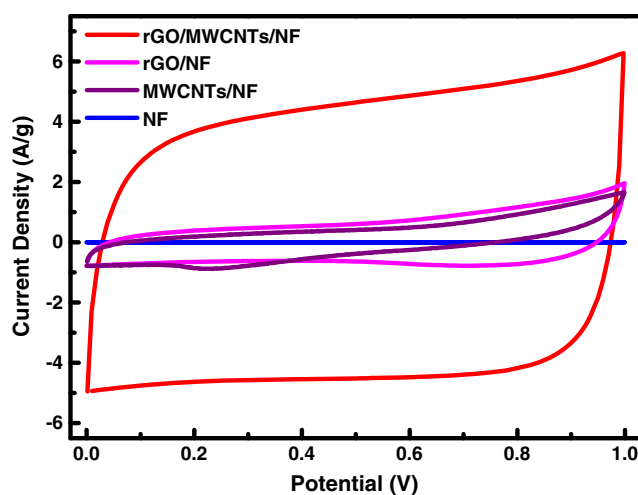
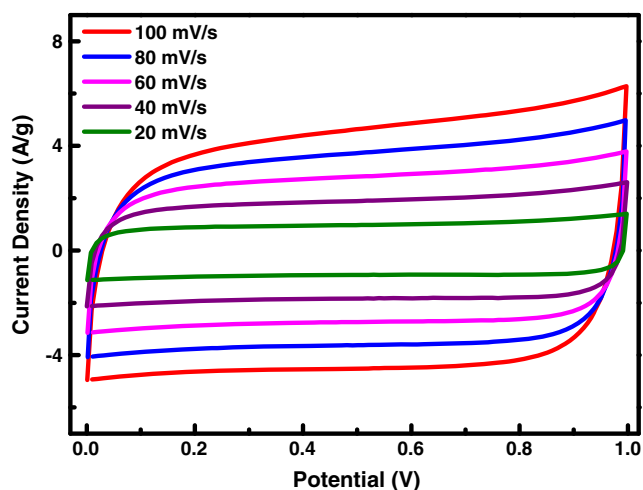


Fig. 7 Cyclic voltammograms recorded for rGO/MWCNTs/NF, rGO/NF, MWCNTs/NF, and bare NF electrodes in 1-M KOH solution at a scan rate of 100  $\text{mV s}^{-1}$

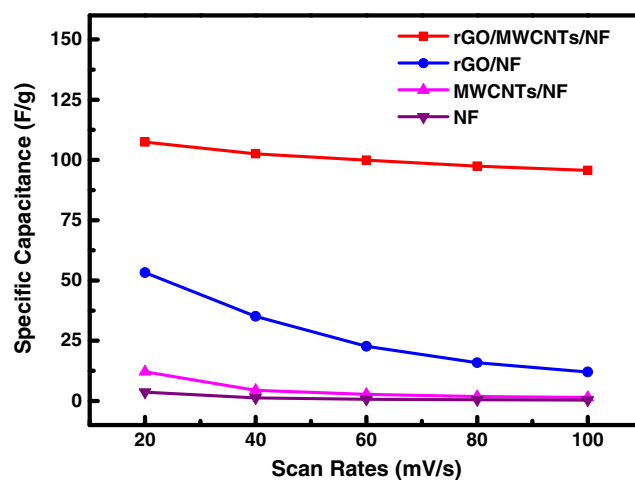


**Fig. 8** Cyclic voltammograms obtained for rGO/MWCNTs/NF electrode in 1-M KOH solution at different scan rates of 20, 40, 60, 80, and 100  $\text{mV s}^{-1}$

with higher current as compared to the rGO/NF, MWCNTs/NF, and bare NF electrodes. The observed cyclic voltammogram for the rGO/MWCNTs/NF electrodes for different scan rates has rectangular shape which indicated ideal double-layer capacitance and good reversibility properties. The higher current observed for rGO/MWCNTs/NF electrode compared to the other electrodes indicating an enhanced electrochemical behavior due to the higher surface area and the increased accessibility of electrolyte ions [27].

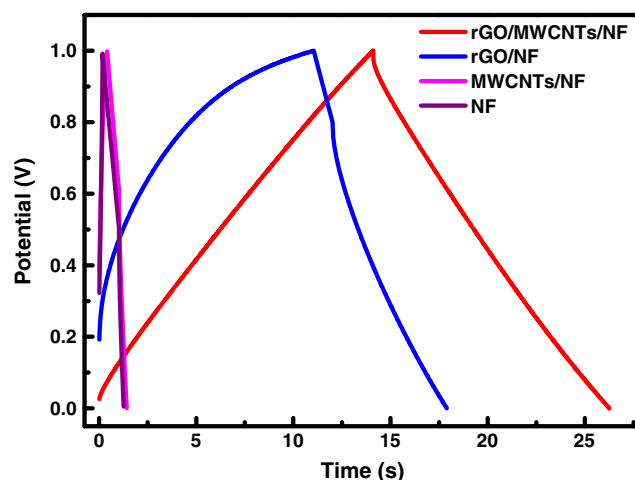
Figure 8 shows the cyclic voltammograms for the rGO/MWCNTs/NF electrode at different scan rates within a potential window from 0 to 1 V. With increasing scan rate, the current response also increases without any obvious changes in the shape of the cyclic voltammogram curve, indicating good electrochemical performance. The rectangular and symmetric shape of the cyclic voltammogram is also observed at a high scan rate of 100  $\text{mV s}^{-1}$  due to the low contact resistance of the electrode.

Figure 9 shows the specific capacitance for rGO/MWCNTs/NF, rGO/NF, MWCNTs/NF, and bare NF electrodes as a function of scan rates. The specific capacitance of the electrodes decreases with the increasing scan rate as shown in Fig. 9. At higher scan rate, the electrochemical reaction occurs only on the electrode/electrolyte interface whereas at slow scan rate, the ions have sufficient time to penetrate into the inner active site of the electrode, which increases the specific capacitance of the electrode. The specific capacitance of the rGO/MWCNTs/NF electrode decreases to small extent of around 12 % with the increasing scan rate. The rGO/NF and MWCNTs/NF electrodes shows larger decrease in specific capacitance with increasing scan rate, when compared to the rGO/MWCNTs/NF electrode. The bare NF electrode shows negligible electrochemical activity when compared to the other electrodes as shown in the Fig. 9. The synthesis of rGO/MWCNTs/NF using hydrothermal method



**Fig. 9** Specific capacitance for rGO/MWCNTs/NF, rGO/NF, MWCNTs/NF, and bare NF electrodes at different scan rates

without any binders, which decreases the internal electrical resistance of the electrode due to the direct contact between the materials, results in a high specific conductance of supercapacitor [49, 50]. The deposition of rGO/MWCNTs composite material on the porous structure of NF provides more accessibility by allowing the electrolyte ions to diffuse more freely during electrochemical reaction. The higher capacitance current of rGO/MWCNTs/NF electrode than that of the rGO/NF, MWCNTs/NF, and bare NF electrodes was observed as shown in the Fig. 8. The enhanced capacitance of rGO/MWCNTs/NF electrode is due to their higher surface area of rGO/MWCNTs/NF composite material, and more accessibility of electrolyte ions [27, 51, 52]. The addition of MWCNTs facilitate the formation of electric double layer by preventing the graphene sheet from restacking while maintaining the specific surface area of graphene sheets. The specific capacitance values calculated from the cyclic voltammogram is 95.7  $\text{F g}^{-1}$  at scan rates of 100  $\text{mV s}^{-1}$ .



**Fig. 10** Galvanostatic charge/discharge curve for rGO/MWCNTs/NF, rGO/NF, MWCNTs/NF, and NF electrodes at the current density of 1  $\text{A g}^{-1}$  in 1-M KOH aqueous solution



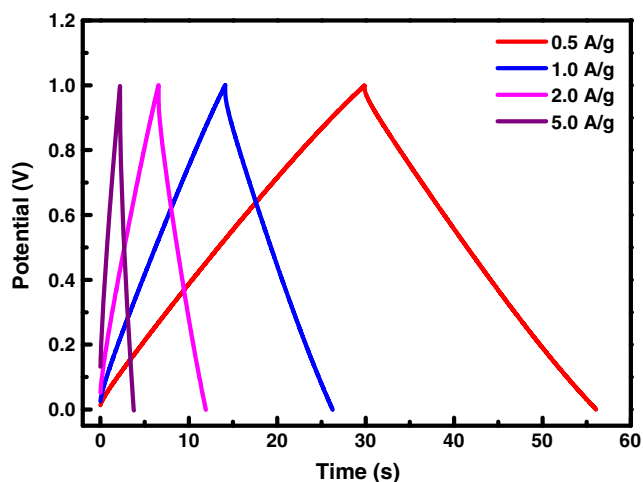


**Fig. 11** Galvanostatic charge/discharge curves for rGO/MWCNTs/NF electrode at different current densities in 1-M KOH aqueous solution

The galvanostatic charge/discharge curve for rGO/MWCNTs/NF, rGO/NF, MWCNTs/NF, and NF electrodes at the current density of  $1 \text{ A g}^{-1}$  in 1-M KOH aqueous solution are shown in Fig. 10. The charge/discharge curves of rGO/MWCNTs/NF, rGO/NF, MWCNTs/NF, and bare NF electrodes almost maintained the similar shape in the potential range from 0 to 1 V. The specific capacitance of rGO/MWCNTs/NF, rGO/NF, and MWCNTs/NF electrodes was calculated to be 81.13, 29.96, and  $13.25 \text{ F g}^{-1}$  at a current density of  $1 \text{ A g}^{-1}$ , respectively. Particularly, the specific capacitance of rGO/NF electrode decreased to  $29.96 \text{ F g}^{-1}$  compared to rGO/MWCNTs/NF electrode, indicating that the addition of MWCNTs plays a significant role for improving the electrochemical performance of the rGO/MWCNTs/NF electrode. The enhanced electrochemical performance of rGO/MWCNTs/NF is due to the unique properties of rGO/MWCNTs/NF composite material and effective uniform sandwich of MWCNTs between the graphene sheets, which

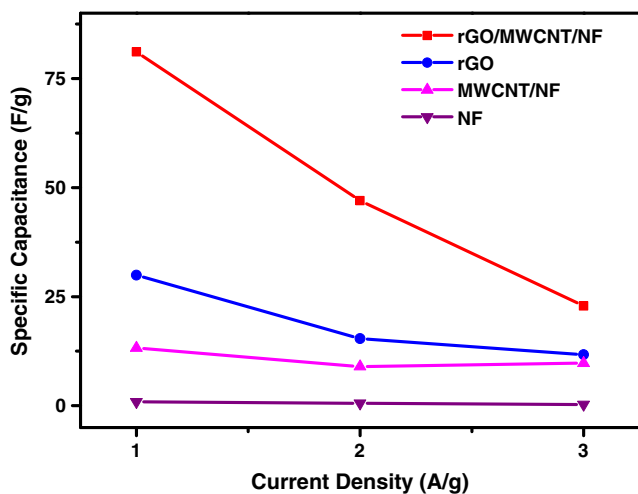


**Fig. 12** Specific capacitance of rGO/MWCNTs/NF, rGO/NF, MWCNTs/NF, and NF electrodes at different current densities

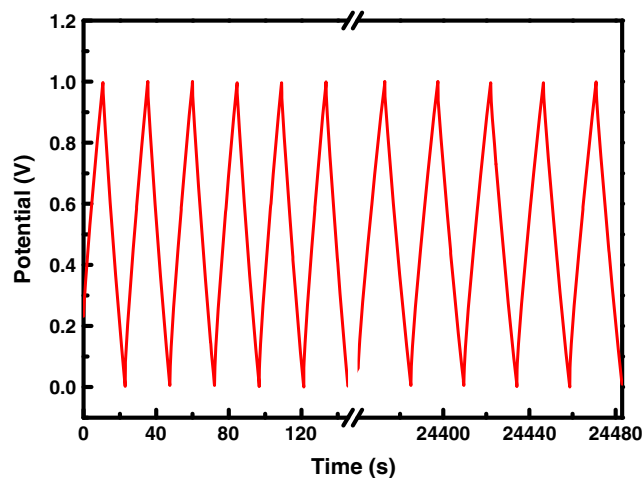


**Fig. 13** The cycling performance of the galvanostatic charge/discharge curves for the rGO/MWCNTs/NF electrode at the current density of  $1 \text{ A g}^{-1}$  in 1-M KOH aqueous solution

increases electrolyte/electrode contact area and facilitates transportation of electrolyte ion and electron into the inner region of electrode [51, 52]. The electrochemical performances of rGO/MWCNTs/NF, rGO/NF, MWCNTs/NF, and NF electrodes obtained from charge/discharge curve shows good agreement with the cyclic voltammetric measurements.

Figure 11 shows the galvanostatic charge/discharge curves of rGO/MWCNTs/NF electrode at different current densities in the potential range from 0 to 1 V. Figure 11 clearly shows that the graph has a symmetrical triangle shape at different current densities. The ions encounter less hindrance during electrochemical reaction after the addition of MWCNTs as shown by more linear charge and discharge curve. The enhanced capacitance of rGO/MWCNTs/NF at  $1 \text{ A g}^{-1}$  is attributed to the unique structure of rGO/MWCNTs/NF composite material with MWCNTs uniformly sandwiched between the graphene sheets, which increases electrolyte/electrode contact

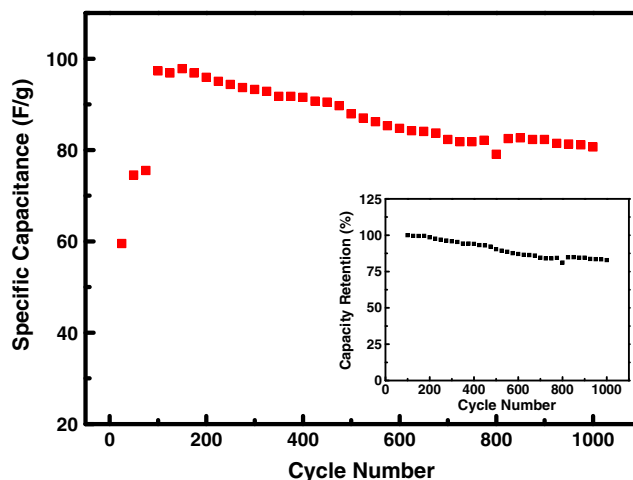


**Fig. 14** The specific capacitance versus the cycle number at a current density of  $1 \text{ A g}^{-1}$ . Inset: capacity retention over 1000 cycles for rGO/MWCNTs/NF electrode

area and facilitates the diffusion of electrolyte ions into the inner region of electrode. The specific capacitances of rGO/MWCNTs/NF, rGO/NF, MWCNTs/NF, and NF electrodes at different current densities are shown in Fig. 12.

The cycling performance of the rGO/MWCNTs/NF electrode at the current density of  $1 \text{ A g}^{-1}$  was also investigated, as shown in Fig. 13. The symmetrical triangle shape still remains unchanged after 1000 cycles of charge and discharge curve (Fig. 13). The specific capacitance of the rGO/MWCNTs/NF electrode changed slightly from  $97.32$  to  $80.65 \text{ F g}^{-1}$  after 1000 cycles (Fig. 14), with more than 83 % of its initial capacitance is maintained, indicating that the rGO/MWCNTs/NF electrode has good stability after 1000 cycles. Figure 14 (inset) shows the capacity retention over 1000 cycles for rGO/MWCNTs/NF electrode with charge/discharge curve from 0 to 1 V. The electrochemical stability test shows that the rGO/MWCNTs/NF electrode remains stable after 1000 cycles.

The improved electrochemical performance demonstrated for the rGO/MWCNTs/NF electrode compared to the other electrodes is due to the large surface area and the more favorable pore volumes. The rGO acts as an effective electronic conductor to facilitate the collection and transportation of electrons during the electrochemical reaction with improving the electronic conductivity of rGO/MWCNTs/NF electrode. Due to the larger surface area owing to its unique structure of rGO/MWCNTs/NF electrode, effectively enhancing the capacitance performance of the rGO/MWCNTs/NF composite material. The larger surface area with porous structure allows for easy diffusion of the electrolyte ions into the inner region of the electrode, reducing diffusion resistance of the electrolyte ions. Binder-free electrodes with a better adhesion reduce Ohmic polarization and enhance the rate capability, and the direct contact between the active material and the electrolyte was favorable for conduction of electrons. The MWCNTs act as spacer between the graphene sheets, which gives free and rapid diffusion of electrolyte ions [27]. As a result, the rGO/MWCNTs/NF electrode exhibited a specific capacitance of  $81.13 \text{ F g}^{-1}$  at a current density of  $1 \text{ A g}^{-1}$  using galvanostatic charge/discharge curve.

## Conclusions

Reduced graphene oxide/multiwalled carbon tubes deposited nickel foam electrode was prepared by simple hydrothermal method without using any binders. The structural and morphological characteristics of the rGO/MWCNTs/NF electrode were studied using scanning electron microscopy and Raman spectroscopy. The capacitive performance of the rGO/MWCNTs/NF electrode was investigated by electrochemical impedance spectroscopy, cyclic voltammetry, and galvanostatic charge/discharge curve in 1 M KOH as electrolyte. The rGO/MWCNTs/NF binder-free electrode exhibited enhanced

capacitance when compared to the rGO/NF, MWCNTs/NF, and bare NF electrodes due to high surface area and more accessibility of electrolyte. The rGO/MWCNTs/NF electrode showed a specific capacitance of  $81.14 \text{ F g}^{-1}$  at current density of  $1 \text{ A g}^{-1}$  and excellent cycling stability with 83 % of its initial capacitance after 1000 charge/discharge cycles, suggesting that the rGO/MWCNTs/NF electrode is a potential candidate for supercapacitor. Hence, the rGO/MWCNTs/NF electrode is promising material for the high-performance supercapacitor electrodes in future.

**Acknowledgments** This work was financially supported by a University of Malaya Research Grant UMRG Programme (RP007C/13AFR), the Science Fund from the Ministry of Science, Technology and Innovation (06-01-04-SF1513), and a High Impact Research Grant from the Ministry of Higher Education of Malaysia (UM.C/625/1/HIR/MOHE/05).

## References

1. B.E. Conway (ed.), *Electrochemical Supercapacitors: Scientific Fundamentals and Technological Applications* (Plenum Publishers, New York, 1999)
2. M.D. Stoller, S. Park, Y. Zhu, J. An, R.S. Ruoff, *Nano Lett.* **8**, 3498 (2008)
3. A. Burke, *J. Power Sources* **91**, 37 (2000)
4. R. Kotz, M. Carlen, *Electrochim. Acta* **45**, 2483 (2000)
5. L. Lai, H. Yang, L. Wang, B.K. Teh, J. Zhong, H. Chou, L. Chen, W. Chen, Z. Shen, R.S. Ruoff, J. Lin, *ACS Nano* **6**, 5941 (2012)
6. L.L. Zhang, X.S. Zhao, *Chem. Soc. Rev.* **38**, 2520 (2009)
7. M. Winter, R.J. Brodd, *Chem. Rev.* **104**, 4245 (2004)
8. M. Grdeń, M. Alsabet, G. Jerkiewicz, *ACS Appl. Mater. Interfaces* **4**, 3012 (2012)
9. J. Drunen, B. Kinkad, M.C.P. Wang, E. Sourty, B.D. Gates, G. Jerkiewicz, *ACS Appl. Mater. Interfaces* **5**, 6712 (2013)
10. Y.-L. Wang, Y.-Q. Zhao, C.-L. Xu, *J. Solid State Electrochem.* **16**, 829 (2012)
11. M. Alsabet, M. Grdeń, G. Jerkiewicz, *Electrocatalysis* **6**, 60 (2015)
12. S. Bose, T. Kuila, A.K. Mishra, R. Rajasekar, N.H. Kim, J.H. Lee, *J. Mater. Chem.* **22**, 767 (2012)
13. Z.-S. Wu, G. Zhou, L.-C. Yin, W. Ren, F. Li, H.-M. Cheng, *Nano Energy* **1**, 107 (2012)
14. H.-J. Choi, S.-M. Jung, J.-M. Seo, D.W. Chang, L. Dai, J.-B. Baek, *Nano Energy* **1**, 534 (2012)
15. D.R. Dreyer, R.S. Ruoff, C.W. Bielawski, *Angew. Chem. Int. Ed.* **49**, 9336 (2010)
16. S. Jayabal, P. Viswanathan, R. Ramaraj, *RSC Adv.* **4**, 33541 (2014)
17. R.R. Salunkhe, Y.-H. Lee, K.-H. Chang, J.-M. Li, P. Simon, J. Tang, N.L. Torad, C.-C. Hu, Y. Yamauchi, *Chem. Eur. J.* **20**, 13838 (2014)
18. W. Deng, X. Ji, M. Gomez-Mingot, F. Lu, Q. Chena, C.E. Banks, *Chem. Commun.* **48**, 2770 (2012)
19. M. Pumera, *Energy Environ. Sci.* **4**, 668 (2011)
20. X. Cao, Z. Yin, H. Zhang, *Energy Environ. Sci.* **7**, 1850 (2014)
21. S.R.C. Vivekchand, C.S. Rout, K.S. Subrahmanyam, A. Govindaraj, C.N.R. Rao, *J. Chem. Sci.* **120**, 9 (2008)
22. L.L. Zhang, R. Zhou, X.S. Zhao, *J. Mater. Chem.* **20**, 5983 (2010)
23. X. Fan, T. Chen, L. Dai, *RSC Adv.* **4**, 36996 (2014)
24. Y. Zhang, M. Ma, J. Yang, W. Huang, X. Dong, *RSC Adv.* **4**, 8466 (2014)
25. D.A.C. Brownson, D.K. Kampouris, C.E. Banks, *J. Power Sources* **196**, 4873 (2011)
26. A.G. Pandolfo, A.F. Hollenkamp, *J. Power Sources* **157**, 11 (2006)



27. Q. Cheng, J. Tang, J. Ma, H. Zhang, N. Shinya, L.-C. Qin, *Phys. Chem. Chem. Phys.* **13**, 17615 (2011)
28. X. Lu, H. Dou, B. Gao, C. Yuan, S. Yang, L. Hao, L. Shen, X. Zhang, *Electrochim. Acta* **56**, 5115 (2011)
29. L. Buglione, M. Pumera, *Electrochem. Commun.* **17**, 45 (2012)
30. L.-Y. Lin, M.-H. Yeh, J.-T. Tsai, Y.-H. Huang, C.-L. Sun, K.-C. Ho, *J. Mater. Chem. A* **1**, 11237 (2013)
31. N. Huang, D.W. Kirk, S.J. Thorpe, C. Liang, L. Xu, W. Li, S. Zhang, M. Sun, *Int. J. Energy Res* (2015). doi:10.1002/er.3246
32. C. Yang, J. Shen, C. Wang, H. Fei, H. Bao, G. Wang, *J. Mater. Chem. A* **2**, 1458 (2014)
33. Y. Bai, M. Du, J. Chang, J. Sun, L. Gao, *J. Mater. Chem. A* **2**, 3834 (2014)
34. J. Yan, T. Wei, Z. Fan, W. Qian, M. Zhang, X. Shen, F. Wei, *J. Power Sources* **195**, 3041 (2010)
35. F. Zeng, Y. Kuang, N. Zhang, Z. Huang, Y. Pan, Z. Hou, H. Zhou, C. Yan, O.G. Schmidt, *J. Power Sources* **247**, 396 (2014)
36. Y. Cheng, S. Lu, H. Zhang, C.V. Varanasi, J. Liu, *Nano Lett.* **12**, 4206 (2012)
37. D. Yu, K. Goh, H. Wang, L. Wei, W. Jiang, Q. Zhang, L. Dai, Y. Chen, *Nat. Nanotechnol.* **9**, 555 (2014)
38. Y. Zhou, N. Lachman, M. Ghaffari, H. Xu, D. Bhattacharya, P. Fattahi, M.R. Abidian, S. Wu, K.K. Gleason, B.L. Wardle, Q.M. Zhang, *J. Mater. Chem. A* **2**, 9964 (2014)
39. F. Wen, C. Hao, J. Xiang, L. Wang, H. Hou, Z. Su, W. Hu, Z. Liu, *Carbon* **75**, 236 (2014)
40. J. Shen, C. Yang, X. Li, G. Wang, *ACS Appl. Mater. Interfaces* **5**, 8467 (2013)
41. Q. Cheng, J. Tang, N. Shinya, L.-C. Qin, *J. Power Sources* **241**, 423 (2013)
42. M.D. Stoller, R.S. Ruoff, *Energy Environ. Sci.* **3**, 1294 (2010)
43. V. Khomenko, E. Frackowiak, F. Beguin, *Electrochim. Acta* **50**, 2499 (2005)
44. W.S. Hummers, R.E. Offeman, *J. Am. Chem. Soc.* **80**, 1339 (1958)
45. H.N. Lim, N.M. Huang, S.S. Lim, I. Harrison, C.H. Chia, *Int. J. Nanomedicine* **6**, 1817 (2011)
46. F. Bao, X. Wang, X. Zhao, Y. Wang, Y. Ji, H. Zhang, X. Liu, *RSC Adv.* **4**, 2393 (2014)
47. L. Li, J. Xu, J. Lei, J. Zhang, F. McLarnon, Z. Wei, N. Li, F. Pan, *J. Mater. Chem. A* **3**, 1953 (2015)
48. X. Dong, B. Li, A. Wei, X. Cao, M.B. Chan-Park, H. Zhang, L.-J. Li, W. Huang, P. Chen, *Carbon* **49**, 2944 (2011)
49. S.-C. Hong, S. Kim, W.-J. Jang, T.-H. Han, J.-P. Hong, J.-S. Oh, T. Hwang, Y. Lee, J.-H. Lee, J.-D. Nam, *RSC Adv.* **4**, 48276 (2014)
50. G. Zhu, Z. He, J. Chen, J. Zhao, X. Feng, Y. Ma, Q. Fan, L. Wang, W. Huang, *Nanoscale* **6**, 1079 (2014)
51. Q. Ke, Y. Liu, H. Liu, Y. Zhang, Y. Hu, J. Wang, *RSC Adv.* **4**, 26398 (2014)
52. Y. Luo, H. Zhang, D. Guo, J. Ma, Q. Li, L. Chen, T. Wang, *Electrochim. Acta* **132**, 332 (2014)